applied sciences

MDPI

Article

Temperature Sensing in Space and Transparent Media: Advancements in Off-Axis Digital Holography and the Temperature Coefficient of Refractive Index

Davood Khodadad [1,*], Behnam Tayebi [2], Amin Saremi [1] and Satyam Paul [3]

[1] Department of Applied Physics and Electronics, Umeå Universitet, 90187 Umeå, Sweden
[2] NYU Grossman School of Medicine, New York, NY 10016, USA
[3] Gas Turbine and Transmissions Research Centre, University of Nottingham, Nottingham NG7 2RD, UK
* Correspondence: davood.khodadad@umu.se

Abstract: An off-axis digital holographic interferometry technique integrated with a Mach–Zehnder interferometer based setup is demonstrated for measuring the temperature and temperature profile of a transparent medium. This technique offers several advantages: it does not require precise optomechanical adjustments or accurate definition of the frequency carrier mask, making it simple and cost-effective. Additionally, high-quality optics are not necessary. The methodology relies on measuring the phase difference between two digitally reconstructed complex wave fields and utilizing the temperature coefficient of the refractive index. In this way, we presented an equation of the temperature as a function of phase changes and the temperature coefficient of refractive index. This approach simplifies the calculation process and avoids the burden of complicated mathematical inversions, such as the inverse Abel transformation. It also eliminates the need for additional work with the Lorentz–Lorentz equation and Gladstone–Dale relation and can be extend for 3D measurements.

Keywords: digital holography; temperature; temperature coefficient of refractive index; space; transparent media; flame; measurement

Citation: Khodadad, D.; Tayebi, B.; Saremi, A.; Paul, S. Temperature Sensing in Space and Transparent Media: Advancements in Off-Axis Digital Holography and the Temperature Coefficient of Refractive Index. *Appl. Sci.* **2023**, *13*, 8423. https://doi.org/10.3390/app13148423

Academic Editor: Andrés Márquez

Received: 12 June 2023
Revised: 9 July 2023
Accepted: 18 July 2023
Published: 21 July 2023

1. Introduction

Temperature measurement plays a crucial role in various fields, including heat transfer, non-isothermal flow, thermal boundary layers, and combustion processes. Accurate temperature measurement plays a vital role in various aspects, including optimizing system design, comprehending physical phenomena, and ensuring the safety of engineering systems. These systems encompass a wide range of applications, such as heat exchangers, aerospace engines, scramjet combustors, and solid propellant plumes. Additionally, temperature measurement is crucial in areas such as turbine operations, the cooling of electronic devices, hot water pipelines, and the food industry. Furthermore, it extends its significance to the advancement of emerging technologies, including sustainable energy, biotechnology, information technology, and nanotechnology [1–6].

Traditional contact methods have limitations in providing full-field temperature data and can influence the measured phenomena, as it is necessary for them to be situated within the experimental domain. Thermocouples, thermometers, resistance temperature detectors, thermistors, and a capacity or change in electrical resistance are typically the predominant types of sensors employed for this purpose. As a result, non-contact methods have gained significant attention because of their non-invasive characteristics and capacity to capture temperature distributions over large areas [7,8].

Non-contact methods for temperature measurement offer several advantages over contact methods, making them desirable in many applications. Firstly, non-contact methods eliminate the need for physical contact with the object or medium being measured, which is particularly advantageous when dealing with delicate or sensitive materials. It

prevents any interference or disruption of the measurement caused by the presence of a sensor or probe. Secondly, non-contact methods provide full-field measurements, allowing temperature mapping over a larger area or volume. This capability is especially beneficial in applications where temperature distribution and gradients are of interest, such as in fluid dynamics, combustion processes, or heat transfer studies. Non-contact methods enable the visualization and analysis of temperature variations across the entire field of view, providing valuable insights into complex thermal phenomena. Furthermore, non-contact techniques offer faster measurement capabilities, enabling real-time or high-speed monitoring of the temperature changes. This is particularly crucial in dynamic processes where the temperature fluctuations occur rapidly or when precise temporal resolution is required.

Additionally, certain non-contact techniques might have constraints in terms of distance, field of view, or environmental factors. For example, thermal imaging methods might be affected by factors such as ambient temperature, air flow, or optical obstructions, leading to potential measurement errors or limitations. Other non-contact techniques for the measurement of the temperature are the spectroscopic method [1], Raman and Rayleigh scattering [9,10], Schlieren photography [11], laser speckle shearing interferometry and photography [12,13], moire deflectometry [14], and interferometric methods, such as holography [15,16], shearing [12–14,17], Talbot [18], and Lau phase [19].

In transparent media, temperature changes induce corresponding refractive index variations, which subsequently affect the phase distribution and variation of a laser beam's wave front passing through the medium [20]. Digital holography provides an advantageous solution for measuring these changes accurately and non-invasively with its differential measurement capabilities. Digital holography allows for the direct collection of the complex amplitude distribution of the wave front in multiple states by dynamically recording a sequence of holograms of the object field at distinct time points [20]. This feature enables the extraction of detailed information, such as the distribution and fluctuation of the refractive index in a transparent medium [21]. Consequently, a two-dimensional map of refractive index changes can be obtained, facilitating highly precise and sensitive temperature calculations.

In the present work, we employ an off-axis digital holographic interferometry technique [22] integrated with a Mach–Zehnder interferometer based setup for temperature measurement of a transparent medium. This technique offers fast measurements and higher accuracy compared with other available interferometry techniques, making it most suitable for our intended purpose. Considering the small size of the flame as a transparent medium in our experiment, the Mach–Zehnder interferometer setup is preferred over the lens-less Fourier Transform digital holography (LLFTDH) as used in [23]. Our experimental layout is simplified and cost-effective compared with the quadriwave lateral shearing interferometer (QWLSI) methods, which require specific two-dimensional gratings [17,24,25]. The measurement speed is limited only by the camera's frame rate and the laser's power, enabling the capture of fast-changing phenomena.

Importantly, the presented method simplifies the calculation process compared with previous approaches [26–31], making it computationally efficient. We calculate the temperature coefficient of the refractive index [32] of air and establish the relationship between the phase changes and temperature variations based on the temperature coefficient of the refractive index. This approach avoids the burden of complicated mathematical inversions, such as the inverse Abel transformation, convolution back projection, iterative reconstruction techniques, as well as additional work with the Lorentz–Lorentz equation [23] and Gladstone–Dale relation [15,33,34].

2. Theory

Consider the object beam as $U_o(x,y) = A_o(x,y)exp(i\varphi_o(x,y))$ and the reference beam in the detector plane as $U_r(x,y) = A_r(x,y)exp(i\varphi_r(x,y))$, respectively, where A represents

the beam's amplitude and ϕ denotes the phase of the respective components. Consequently, the resulting image intensity recorded, denoted as $I(x, y)$, can be expressed as

$$I(x,y) = A_o^2(x,y) + A_r^2(x,y) + A_r A_o((x,y)exp(i\Delta\varphi) + A_r A_o(x,y)exp(-i\Delta\varphi) \quad (1)$$

In Equation (1), we assume $A_r(x, y) = A_r$ to be a constant value, and $\Delta\varphi = \varphi_o(x, y) - \varphi_r(x, y)$ represents the phase difference between the object beam $U_o(x, y)$ and the reference beam $U_r(x, y)$. Equation (1)'s first two intensity components relate to the zero order and gradual variations across the detector. The remaining two components correspond to the interference terms, which are highly responsive to changes in $\Delta\varphi$. Modifying the size of the aperture allows for the adjustment of the spatial frequency content of the interference terms. Further, adjusting the incidence angle allows the interference component to be positioned at various positions in the Fourier domain.

In our analysis, we focus on the third term in Equation (1), denoted as $J(x, y) = U_o(x, y)U_r^*(x, y) = A_r A_o exp(i\Delta\varphi)$. We assume that the reference beam $U_r(x, y)$ primarily captures the variations in phase φ caused by the tilt angle and curvature of the field across the detector. For digitally recorded holograms, we utilize $\breve{U}_{rd}(x, y)$ as a simplified approximation of the actual experimental reference beam $U_r(x, y)$ during the reconstruction process [35]. $\breve{U}_{rd}(x, y)$ can be presented as

$$\breve{U}_{rd}(x,y) = \left|\breve{U}_{rd}(x,y)\right| exp\left[i\frac{2\pi}{\lambda}\left(ax + by + c(x^2 + y^2)\right)\right]. \quad (2)$$

In this context, λ represents the wavelength of the laser beam used. It is important to note that the symbol $\breve{}$ signifies a computed version of the hologram, obtained through numerical reconstruction methods. Based on the two-dimensional Fourier transform properties

$$f(x,y)exp(i2\pi(ax + by)) \Leftrightarrow F(s_x - a, s_y - b). \quad (3)$$

In Equation (3), (x, y) represents the point coordinates in the spatial domain, while (s_x, s_y) represents the point coordinates in the spectral domain. The term $ax + by$ in the equation signifies the displacement of the object carrier frequency center in the Fourier domain. This displacement is attributed to the off-axis positioning of the reference beam $U_r(x, y)$. In addition, the term $c(x^2 + y^2)$ in Equation (2) represents the curvature of the reference beam $U_r(x, y)$. The curvature of the beam functions as a positive lens on $U_o(x, y)$, effectively creating a focal length equivalent to the distance between the point source of the reference beam $U_r(x, y)$ and the detector [36]. This ensures a consistent magnification for the refocused holograms, maintaining a uniform scaling factor throughout the imaging process. Consequently, we will proceed with the assumption that the amplitude of the reference beam $|U_r(x, y)|$ remains constant and can be disregarded in subsequent discussions.

As a result, we obtain a reconstructed version of the object beam $\breve{U}_o(x, y)$ as

$$\breve{U}_o(x,y) = \breve{J}(x,y).\frac{\breve{U}_{rd}(x,y)}{\left|\breve{U}_{rd}(x,y)\right|^2}, \quad (4)$$

where $\breve{U}_{rd}$(x, y) is determined by Equation (2). When correctly defined, it becomes independent of the optical path length of the reference beam $U_r(x, y)$. The multiplication of the $\breve{J}(x, y)$ term by $\breve{U}_{rd}$(x, y)/ $|\breve{U}_{rd}$(x, y)$|^2$ aims to simulate the illumination of the hologram during the reconstruction process in classical holography by a replica of $U_r(x, y)$. Obviously, when $U_r(x, y) = \breve{U}_{rd}(x, y)$, $\breve{U}_o(x, y)$ will be retrieved [35,37].

When the complex field $\breve{U}_o(x, y)$ is retrieved as an object information, the phase information of $\breve{U}_o(x, y)$ can be calculated as

$$\varphi(x,y) = \mathrm{Arg}\left(\breve{U}_o(x,y)\right) = \arctan\frac{Im\left(\breve{U}_o(x,y)\right)}{Re\left(\breve{U}_o(x,y)\right)} \quad (5)$$

The phase information may be wrapped within the interval of $[-\pi, +\pi]$ radians due to the principles of the arctan function. However, it is important to note that the actual phase may vary over the range of 2π.

When a laser beam propagates through transparent media (e.g., a flame) in a parallel manner, the phase of the object wave front changes, due to the change of temperature and consequently change of refractive index inside the media [20]. The phase differences can be reconstructed numerically from the retrieved digital hologram $\check{U}_o(x, y)$, as is stated in Equation (5). In the digital holography set up, at least two digital holograms should be captured in order to measure the temperature variations. The first hologram corresponds to the reference or initial state of the temperature, and the second hologram is recorded when the temperature field has been changed. If the two holograms are recorded separately and their phase information is calculated, the phase difference $\Delta\varphi(x, y)$ by a modulo of 2π subtraction provides information on the refractive index change occurring between the two states, which relates to the temperature field variations.

$$\Delta\varphi(x, y) = \begin{cases} \varphi_1 - \varphi_2 \text{ if } \varphi_1 \geq \varphi_2 \\ \varphi_1 - \varphi_2 + 2\pi \text{ if } \varphi_1 < \varphi_2 \end{cases}, \tag{6}$$

where φ_1 and φ_2 are the phase distribution of the holograms at the reference state and measurement state, respectively. Let us assume the first hologram (reference) is recorded at the time t_1, with refractive index n_1, and the second hologram at the time t_2 with n_2. The phase change $\Delta\varphi$ between two states of the hologram originates from the change in optical path length (OPL), ΔOPL. So, $\Delta\varphi(x, y)$ can be written as [20,38]

$$\Delta\varphi(x, y) = \frac{2\pi}{\lambda}\Delta OPL. \tag{7}$$

However, ΔOPL originates from the change of refractive index and can be calculated as [20]

$$\Delta OPL = \int_{L_1}^{L_2} \Delta n(x, y, z)dz,$$

where $\Delta n(x, y, z)$ denotes the change of the refractive index in the measured volume. For the temperature change $\Delta T = T_{t_2} - T_{t_1}$, the relation between $\Delta\varphi$ and the refractive index variation $\Delta n = n_2 - n_1$ can be derived by altering the ΔOPL with the index variation of the transparent media in Equation (7). So, Equation (7) can be expressed as [20]

$$\Delta\varphi(x, y) = \frac{2\pi}{\lambda}\int_{L_1}^{L_2} \Delta n(x, y, z)dz. \tag{8}$$

In our analysis, we work with a three-dimensional representation using X, Y, and Z axes. The optical axis aligns with the Z-axis, representing the direction of the optical path. To simplify the study and for the case of a 2D temperature field, we focus on the 2D plane (X, Y) perpendicular to the optical axis. This choice allows us to assume that the temperature variation occurs only within this plane. So, a constant temperature is assumed in the direction of the optical axis, while the refractive index changes in the X and Y directions but remains constant along the optical axis. Consequently, Equation (8) simplifies then to

$$\Delta\varphi(x, y) = \frac{2\pi}{\lambda}L\Delta n, \tag{9}$$

where $L = L_2 - L_1$ denotes the differential distance that the beam passes through the medium (the total length of the media).

Equation (9) can be written as

$$\frac{\Delta\varphi(x, y)}{\Delta T} = \frac{2\pi}{\lambda}L\frac{\Delta n}{\Delta T} \tag{10}$$

So, the temperature variations can be related to $\frac{dn}{dT}$ as

$$\Delta T = \frac{\Delta\varphi(x,y)\lambda}{2\pi L\frac{dn}{dT}} \tag{11}$$

where $\frac{dn}{dT}$ is thermal coefficients of the air refractive index as a ratio of changes of the refractive index to the changes of temperature [39–41].

So, the temperature can be found as:

$$T_{t_2} = T_{t_1} + \frac{\Delta\varphi(x,y)\lambda}{2\pi L\frac{dn}{dT}} \tag{12}$$

The refractive index of air for the wavelength range 230 nm $\leq \lambda \leq$ 1630 nm and the temperature of T with the pressure of P can be calculated with good accuracy [42] with

$$n_{air}(\lambda, T, P) = 1 + \frac{P}{P_0} \times \frac{n_{air}(\lambda, T = 15\ ^\circ\mathrm{C}, P_0) - 1}{1 + 3.478 \times 10^{-3}\frac{1}{^\circ\mathrm{C}} \times (T - 15\ ^\circ\mathrm{C})} \tag{13}$$

where $n_{air}(\lambda, T = 15\ ^\circ\mathrm{C}, P_0)$ is the reference refractive index of the air at the temperature of T = 15 °C with a pressure of 1 atmosphere, P_0 = 101325 N/m^2, which for the wavelength λ can be calculated as [42]

$$n_{air}(\lambda, 15\ ^\circ\mathrm{C}, P_0) = 1 + 10^{-8} \times \left[6432.8 + \frac{2949810\frac{1}{\mu m^2}\lambda^2}{146\frac{1}{\mu m^2}\lambda^2 - 1} + \frac{25540\frac{1}{\mu m^2}\lambda^2}{41\frac{1}{\mu m^2}\lambda^2 - 1}\right] \tag{14}$$

Using Equations (13) and (14), the thermal coefficients of the air refractive index can be expressed as

$$\frac{dn_{air}(\lambda, T, P)}{dT} = -0.00367\frac{n_{air}(\lambda, T, P) - 1}{1 + 0.00367\frac{1}{^\circ\mathrm{C}}T} \tag{15}$$

So, by knowing the wavelength of the laser source, which was λ = 531.8 nm in our experiment, $n_{air}(531.8\ \mathrm{nm}, 15\ ^\circ\mathrm{C}, P_0)$ becomes 1.00027259905. Further, the thermal coefficient of the refractive index for the λ = 531.8 nm at T = 15°C is then determined as

$$\frac{dn_{air}}{dT} = -9.4824 \times 10^{-7}.$$

3. Experimental Investigation

Figure 1 illustrates the schematic of the Mach–Zehnder off-axis digital holographic setup used to measure temperature variations of a candle flame as a test transparent medium. The experiment was carried out at the temperature of 15 °C and 1 atm pressure. In this experiment, we used Thorlab's CPS532-C2 collimated laser-diode-pumped DPSS laser module with a wavelength of 531.8 nm and an output power of 0.9 mW as the light source. The laser beam is split into two parts using a cubic beam splitter (BS). In this setup, a portion of the laser beam is designated as the reference beam, while another portion of the beam functions as the object beam. The object beam is diverged by a negative lens and passes through the test object (candle flame) and another cubic beam splitter before reaching the digital camera (FLIR-BFS-U3-120S4M-CS Monochrome Camera). The negative lens is used to illuminate a larger area of the flame. The reference beam is directed towards the camera at a small angle after passing through an ND filter, reflecting off a mirror, and passing through the cubic beam splitter. The mirror can be adjusted to provide a suitable small angle between the reference and object beams. The object and reference beams interfere at the camera sensor, and a complex hologram image is captured. The camera features a Sony IMX226 imaging sensor composed of 4000 × 3000 pixels, with each pixel measuring 1.85 µm × 1.85 µm. The camera's sensing area is 7.4 mm × 5.55 mm with 31 fps.

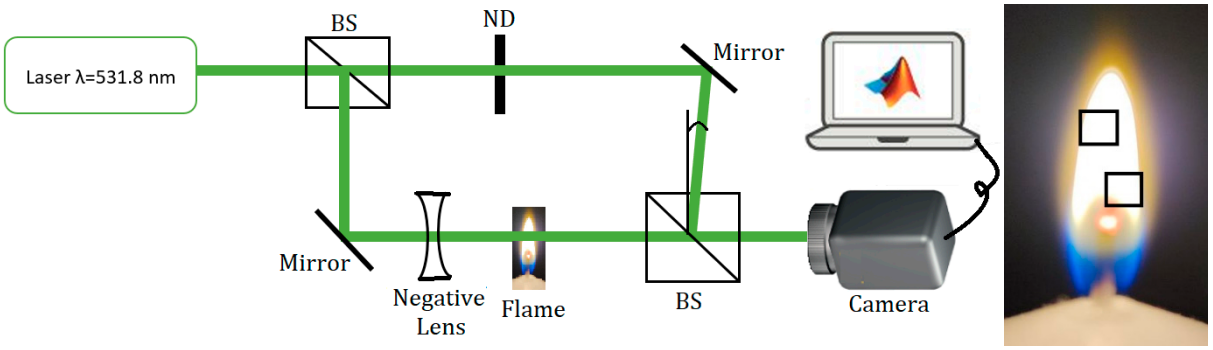

Figure 1. Schematic of the experimental setup Mach–Zehnder interferometer off-axis digital holography (**right**) and the test object (**left**). BS and ND represent beam splitter and neutral density filter, respectively. The two rectangles on the candle flame indicate the area where temperature measurements were taken within the (X, Y) plane, perpendicular to the optical path axis Z.

First, a complex holographic image was captured without a candle flame (representing the air) and kept as a reference image for lateral calibration issues. Then, multiple images were captured corresponding to different states of the air's refractive index due to the candle flame and variations in the flame's temperature. Image reconstruction and relevant post-processing algorithms were implemented using MATLAB R2021b software.

The first step of the reconstruction procedure involves removing the zero-order term from the recorded hologram. We apply a method described in [37]. A spatial frequency mask is applied in the Fourier domain to select only the carrier frequencies that contain the required hologram information. The mask's size and shape are chosen to cover only one of the carrier frequencies of the twin lobes in the spectral domain (Figure 2), effectively filtering out all frequencies except the desired ones. The chosen frequencies are then cantered and zero-padded in the Fourier domain. The complex image $\breve{U}_o(x, y)$ is retrieved using the inverse fast Fourier transform.

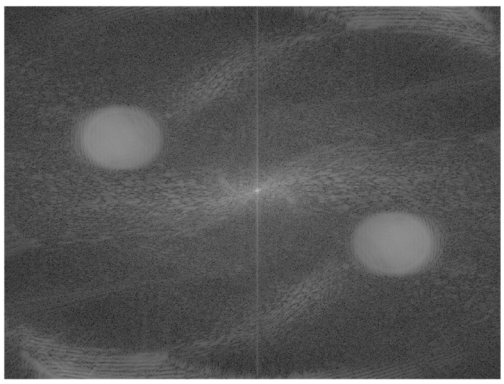

Figure 2. The spectrum of the recorded hologram.

The phase distribution of the reconstructed images can be calculated using Equation (5). However, in addition to the dynamically varying phase changes caused by temperature variations, some pseudo phase can be introduced in the derived phase information. This pseudo phase change may originate from wave front and optical element aberrations, improper selection of the Fourier mask for carrier frequencies, or the residual effect of the reference wave tilt angle [35,43]. However, in this setup, the phase changes between two states of the object will carry the same pseudo phase due to the shared source of aberrations. Therefore, using Equation (6) to calculate the phase changes cancels out the existing aberrations, and the final measured phase changes remain unaffected. Utilizing the reference image is beneficial, as it eliminates the need for precise optomechanical adjustments and accurate definition of the frequency carrier mask. However, there are always time-variant

phase aberrations. Thus, the reference image should be captured shortly before capturing images of the dynamic phenomenon to minimize the impact of time-variant environmental factors on the measurements. Generally, subtracting the reference image can eliminate a significant amount of phase aberrations [44]. However, residual aberrations may persist, necessitating additional approaches for further minimization. Numerical methods, such as those discussed in references [43,45], offer a promising avenue for addressing these remaining aberrations. Specifically, in multiplexed holography, a small misalignment in the centers of the frequency masks, arising from pixel size localization accuracy, can be compensated by defining a numerical digital reference wave [35] to minimize phase aberrations. Similarly, wave front distortions can be mitigated through the utilization of numerical digital reference waves. These methods enhance the efficacy of subtracting the reference image in reducing aberrations and contribute to the optimization of holographic reconstruction quality.

4. Result and Discussion

A reference hologram of air without a candle flame was recorded and is shown in Figure 3. The interference pattern includes the information of both the reference beam and the object beam passing through the air. The direction of the interference fringes can indicate the tilt angle between the reference beam and the object beam. This direction is also related to the direction of the twin side lobes in the Fourier domain, as can be seen in the spectrum of the recorded hologram in Figure 2. The hologram was reconstructed using the numerical reconstruction method described in the previous section. The phase distribution map of the reference hologram was then extracted using Equation (5), revealing the wrapped phase representation shown in Figure 4 (left). This wrapped phase map demonstrates a periodicity of 2π modulo (due to the nature of the arctan function).

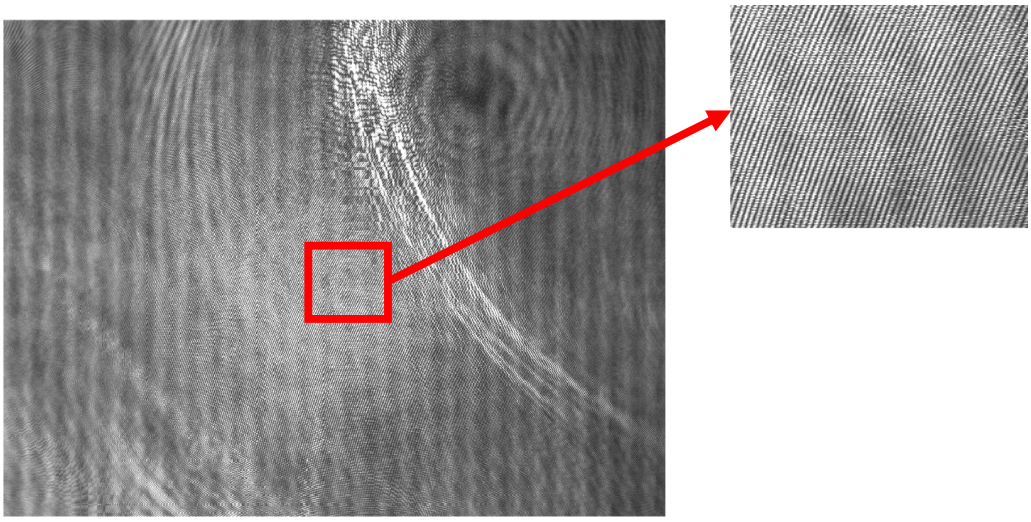

Figure 3. The captured reference hologram displays the interference pattern, which is visible in the scaled region.

Another hologram was recorded from the candle flame from the area corresponding to the rectangle indicated at the bottom of Figure 1. Using the same reconstruction procedure, the hologram of the candle flame was reconstructed, and the phase distribution was calculated (Figure 4 (left)). The phase difference between the holograms with and without the flame was then computed using Equation (6) and is shown in Figure 5. It is important to note that the frequency carrier mask should remain unchanged for the entire hologram reconstruction procedure.

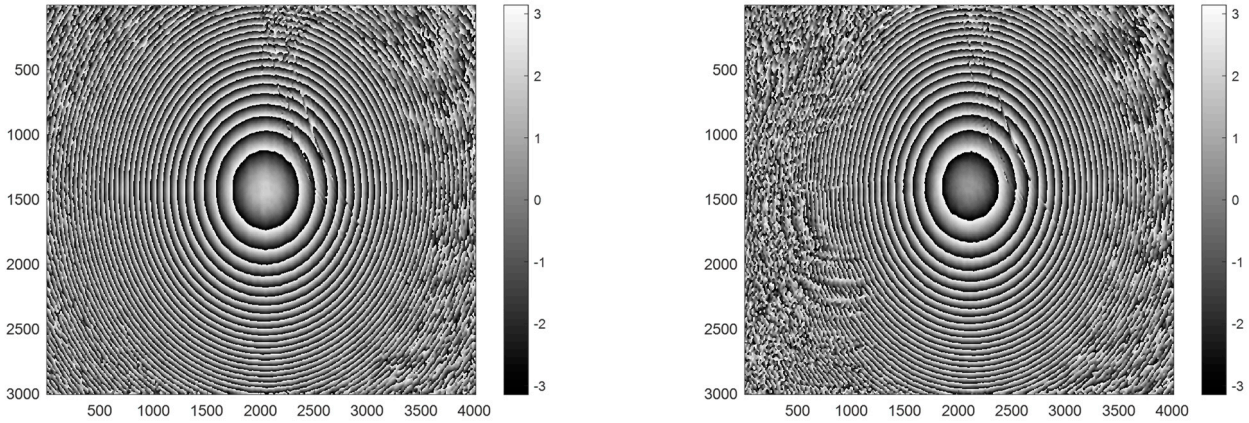

Figure 4. Phase distribution for the reference hologram (**left**) and for the measurement hologram with the flame (**right**), corresponding to the rectangular area at the bottom of the flame (Figure 1, (right)).

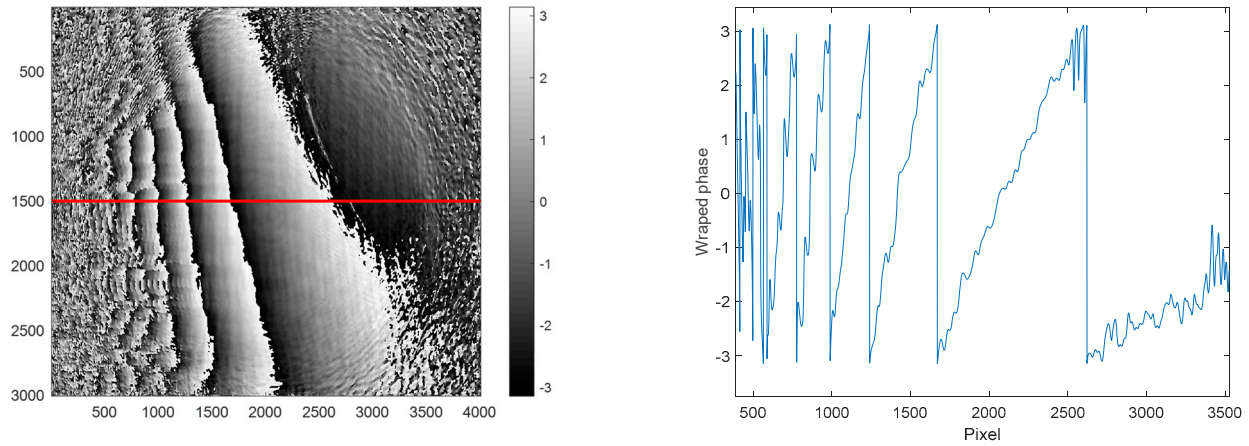

Figure 5. Phase change map (**left**) and a cross-sectional profile plot at pixel row number 1500 (**right**). The red line indicates the pixels chosen for the cross-sectional profile.

As observed, the phase change map wraps quickly on the left side and gradually becomes slower from left to right. The hologram quality is higher in the interval from pixel number 500 to 3500 on the horizontal axis, where the results are shown and discussed. So, a cross-sectional profile plot of the phase difference map at pixel row number 1500 (red line) was chosen and plotted in Figure 5 (left). The line profile of the wrapped phase indeed reaches minima at positions that correspond to dark fringes. In Figure 6 (left), the unwrapped phase changes of the chosen line are plotted. The unwrapped phase initially decreases and then sharply increases until the end. The slope of the increment decreases as it moves towards the right. Using Equation (9), the refractive index differences are also plotted and shown in Figure 6. Similar to the phase changes, the refractive index first decreases, changes slope, and then sharply increases until it reaches the end, becoming smoother. The change in the refractive index is proportional to the phase difference with a proportionality coefficient factor of $2\pi L/\lambda$. By using the relation introduced in Equation (12), the temperature variation is calculated and plotted in Figure 6, left. Contrary to the refractive index and phase changes, as we move away from the center towards the outer region of the flame, the temperature first increases from 575 °C to almost 650 °C and then gradually decreases until the end.

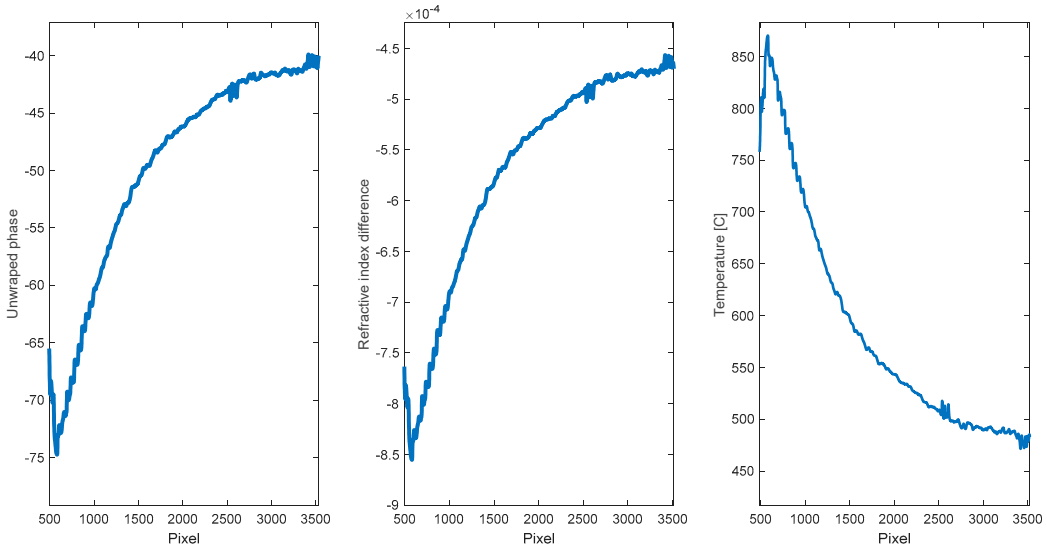

Figure 6. Unwrapped phase change (**left**), refractive index difference (**centre**), and the calculated temperature (**right**), corresponding to the rectangular area indicated at the bottom of the flame (Figure 1, right).

Figures 4–6 depict the progressive implementation of the proposed method outlined in the theoretical section, as elucidated by Equations (5)–(15). These figures demonstrate the step-by-step flow of the methodology, visually illustrating the application of the theoretical principles discussed. By sequentially presenting the results in Figures 4–6, we provide a comprehensive and tangible representation of the proposed approach.

Another hologram was recorded from the rectangular area indicated at the top of the flame, as shown in Figure 1 (right). The extracted phase map of the corresponding area is displayed in Figure 7 (right), while the phase difference map between the hologram with and without the flame is presented in Figure 7 (left). The phase difference wraps more quickly than the phase difference shown in Figure 5. Consequently, according to Equation (9), the refractive index changes more quickly. Similarly, a cross-sectional profile plot of the phase difference map at pixel row number 1500 (red line) was chosen and plotted in Figure 8. The wrapped phase was unwrapped and shown in Figure 9. The corresponding refractive index difference was calculated and plotted in Figure 9 (centre). As expected from Equation (9), the phase changes and the refractive index follow the same trend. The temperature changes are shown in Figure 9 (right).

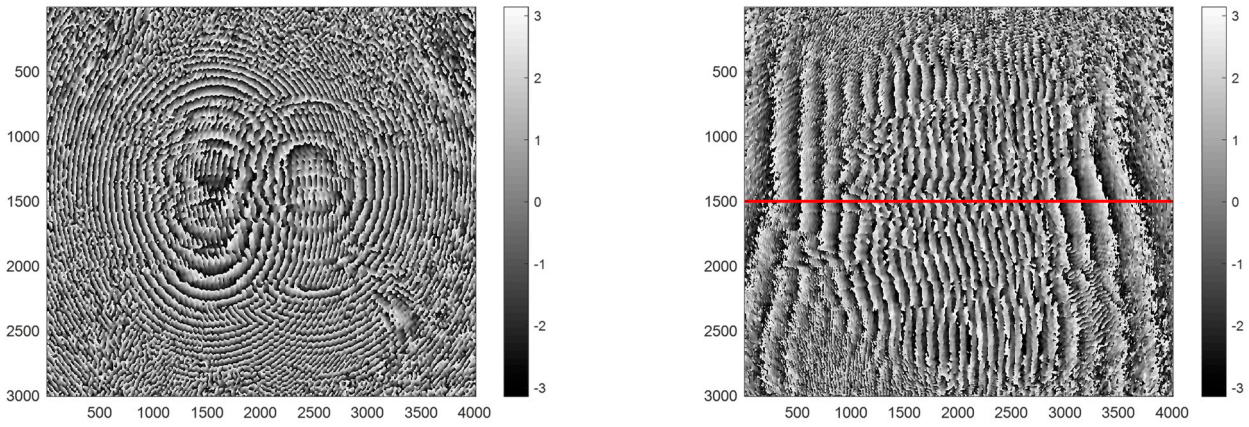

Figure 7. Extracted phase (**left**) and phase difference maps (**right**) for the rectangular area indicated at the top of the flame (Figure 1, right). The red line indicates the pixels chosen for the cross-sectional profile.

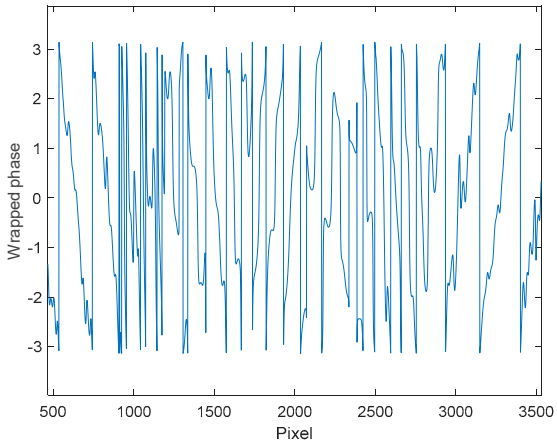

Figure 8. A cross-sectional profile plot of the phase difference map (Figure 7, right) at pixel row number 1500 (the red line).

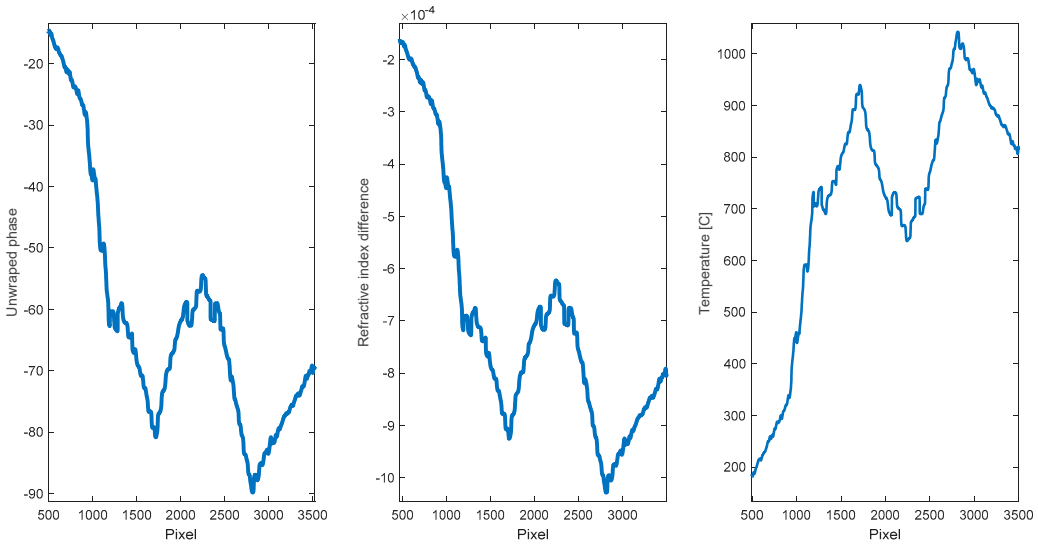

Figure 9. Unwrapped phase change (**left**), refractive index difference (**centre**), and the calculated temperature (**right**) for the rectangular area indicated at the top of the flame (Figure 1, right).

In this region, the temperature exhibits two maxima around the flame's center. Specifically, in the surrounding areas of the flame's center, the temperature increases. As we move from the center towards the outer region of the flame, the temperature first increases and reaches a maximum. Then, it sharply decreases until reaching the outer region of the flame.

The temperature distribution of a candle flame is influenced by various parameters, including the type of oil wax and wick thickness [28,29]. Previous studies have reported peak temperatures ranging from 600 °C to 2000 °C for candle flames [23,24,28,29,46–48]. Additionally, temperature profiles along the radial distance at different heights have shown variations in temperature. The literature consistently demonstrates that the hottest zone of the candle flame is located around the flame's center, with the hottest location gradually shifting closer to the center as the height increases. Moreover, an interesting observation is the existence of a local minimum at the center of the flame, accompanied by two peaks of temperature [23,24,28,29].

In our experimental investigation, as shown in Figures 6 and 9, we have observed patterns that support the aforementioned findings similar to those in [23,24,28,29,46–48]. Specifically, in Figure 6 (right) and Figure 9 (right), we present our measured temperature profiles, where the peak temperature is located around the flame's center. Notably, the left part of Figure 6 (right), corresponding to the position near the central position of the flame,

exhibits the closest proximity of the peak temperature to the flame's center. In Figure 9 (right), we observe a temperature profile with a local minimum at the center of the flame, flanked by two peaks of temperature. These experimental observations are in accordance with the reported measurements documented in [23,24,28,29,46–48].

From Equation (11), the estimation of temperature measurement uncertainty can be derived by considering the uncertainties associated with individual parameters involved in the measurement process. Assuming that only the uncertainty of the wavelength ε_λ and the uncertainty of the phase change $\varepsilon_{\Delta\varphi}$ contribute to the overall temperature measurement and are independent of each other, the uncertainty of the measurement can be expressed as

$$\varepsilon_{\Delta T} = \frac{1}{2\pi L(9.4824 \times 10^{-7})} \sqrt{(\Delta\varphi\varepsilon_\lambda)^2 + (\lambda\varepsilon_{\Delta\varphi})^2} \tag{16}$$

If we substitute the maximum uncertainty of the wavelength of the laser source as $\varepsilon_\lambda = 0.1$ nm and the phase change uncertainty as $\varepsilon_{\Delta\varphi} = \frac{\pi}{5}$ and consider $L = 7.4$ mm as well as $\Delta\varphi = 10\pi$ and 25π for the first and second measurement holograms, the uncertainty of measuring the temperature change becomes approximately 0.93 °C. This level of accuracy is comparable to the reported range of 0.5 °C to 5 °C for the QWLSI method [17,24].

5. Conclusions

In conclusion, we have successfully demonstrated an off-axis digital holographic interferometry technique integrated with a Mach–Zehnder interferometer based setup for precise temperature measurement and profiling of transparent media. This technique offers numerous advantages, including its simplicity, cost-effectiveness, and independence from precise optomechanical adjustments and accurate frequency carrier mask definition. Furthermore, it does not require high-quality optics or specific two-dimensional gratings.

The core principle of the technique lies in measuring the phase difference between two digitally reconstructed wave fields and leveraging the temperature coefficient of the refractive index. Through this approach, we derived Equation (12) that relates temperature to phase changes and the temperature coefficient of the refractive index. Equation (12) simplifies the calculation process and eliminates the need for complex mathematical inversions, such as the inverse Abel transformation. It also removes the requirement for additional computations involving the Lorentz–Lorentz equation and Gladstone–Dale relation. Moreover, the technique has the potential to be extended for 3D measurements. In order to use Equation (12), which relates the temperature to the phase changes, it is essential to have the thermal coefficient of the refractive index. This coefficient is provided by Equation (16), which incorporates the necessary information regarding the corresponding temperature, pressure, and wavelength. Thus, Equation (16) plays a crucial role in obtaining the thermal coefficient required for accurate temperature calculations using Equation (12).

By estimating the uncertainty of the measurement to be less than 1 °C, we have demonstrated the high precision achievable with this technique. The measurement speed depends primarily on the camera's frame rate and the laser's power, enabling the capture of fast-changing phenomena.

Overall, this off-axis digital holographic interferometry technique integrated with a Mach–Zehnder interferometer based setup offers a reliable and efficient solution for temperature measurement in transparent media, opening up possibilities for various applications in research and industry, such as combustion studies, emissions control, fire safety, aerospace and propulsion systems, and environmental research.

Author Contributions: Conceptualization, D.K.; Methodology, D.K.; Formal analysis, D.K.; Data curation, D.K.; Writing—original draft, D.K.; Writing—review & editing, D.K., B.T., A.S. and S.P.; Visualization, D.K., B.T., A.S. and S.P. All authors have read and agreed to the published version of the manuscript.

Funding: This research received no external funding.

Institutional Review Board Statement: Not applicable.

Informed Consent Statement: Not applicable.

Data Availability Statement: Data available upon request.

Conflicts of Interest: The authors declare no conflict of interest.

References

1. Childs, P.R.; Greenwood, J.; Long, C. Review of temperature measurement. *Rev. Sci. Instrum.* **2000**, *71*, 2959–2978. [CrossRef]
2. Parigger, C.G.; Woods, A.C.; Surmick, D.M.; Donaldson, A.B.; Height, J.L. Aluminum Flame Temperature Measurements in Solid Propellant Combustion. *Appl. Spectrosc.* **2014**, *68*, 362–366. Available online: https://opg.optica.org/as/abstract.cfm?URI=as-68-3-362 (accessed on 1 May 2023). [CrossRef]
3. Chen, Y.; Guildenbecher, D.R.; Hoffmeister, K.N.G.; Cooper, M.A.; Stauffacher, H.L.; Oliver, M.S.; Washburn, E.B. Study of aluminum particle combustion in solid propellant plumes using digital in-line holography and imaging pyrometry. *Combust. Flame* **2017**, *182*, 225–237. [CrossRef]
4. McGee, T.D. *Principles and Methods of Temperature Measurement*; John Wiley & Sons: Hoboken, NJ, USA, 1988.
5. Ross-Pinnock, D.; Maropoulos, P.G. Review of industrial temperature measurement technologies and research priorities for the thermal characterisation of the factories of the future. *Proc. Inst. Mech. Eng. Part B J. Eng. Manuf.* **2016**, *230*, 793–806. [CrossRef]
6. Osornio-Rios, R.A.; Antonino-Daviu, J.A.; Romero-Troncoso, R.d.J. Recent Industrial Applications of Infrared Thermography: A Review. *IEEE Trans. Ind. Inform.* **2019**, *15*, 615–625. [CrossRef]
7. Rai, V.K. Temperature sensors and optical sensors. *Appl. Phys. B* **2007**, *88*, 297–303. [CrossRef]
8. Arman Kuzubasoglu, B.; Kursun Bahadir, S. Flexible temperature sensors: A review. *Sens. Actuators A Phys.* **2020**, *315*, 112282. [CrossRef]
9. Haumann, J.; Leipertz, A. Flame-temperature measurements using the Rayleigh scattering photon-correlation technique. *Opt. Lett.* **1984**, *9*, 487–489. [CrossRef] [PubMed]
10. Wehrmeyer, J.A.; Cheng, T.-S.; Pitz, R.W. Raman scattering measurements in flames using a tunable KrF laser. *Appl. Opt.* **1992**, *31*, 1495–1504. [CrossRef]
11. Iffa, E.; Aziz, A.; Malik, A. Gas flame temperature measurement using background oriented schlieren. *J. Appl. Sci.* **2011**, *11*, 1658–1662. [CrossRef]
12. Farrell, P.V.; Hofeldt, D.L. Temperature measurement in gases using speckle photography. *Appl. Opt.* **1984**, *23*, 1055–1059. [CrossRef] [PubMed]
13. Shakher, C.; Nirala, A.K. Measurement of temperature using speckle shearing interferometry. *Appl. Opt.* **1994**, *33*, 2125–2127. [CrossRef]
14. Keren, E.; Bar-Ziv, E.; Glatt, I.; Kafri, O. Measurements of temperature distribution of flames by moiré deflectometry. *Appl. Opt.* **1981**, *20*, 4263–4266. [CrossRef] [PubMed]
15. Rastogi, V.; Kumar, V.; Dubey, S.K.; Khan, G.S.; Shakher, C. Noncontact temperature measurement of human hand skin using volume phase holographic optical element based digital holographic interferometer. *Opt. Lasers Eng.* **2022**, *151*, 106886. [CrossRef]
16. Agarwal, S.; Kumar, V.; Shakher, C. Temperature measurement of wick stabilized micro diffusion flame under the influence of magnetic field using digital holographic interferometry. *Opt. Lasers Eng.* **2018**, *102*, 161–169. [CrossRef]
17. Cui, B.-C.; Wang, J.-L.; Yao, K.-N.; Chen, T. Measurement of high-dynamic temperature field using high-speed quadriwave lateral shearing interferometer. *Optoelectron. Lett.* **2018**, *14*, 124–128. [CrossRef]
18. Shakher, C.; Daniel, A.P. Talbot interferometer with circular gratings for the measurement of temperature in axisymmetric gaseous flames. *Appl. Opt.* **1994**, *33*, 6068–6072. [CrossRef]
19. Thakur, M.; Vyas, A.; Shakher, C. Measurement of temperature and temperature profile of an axisymmetric gaseous flames using Lau phase interferometer with linear gratings. *Opt. Lasers Eng.* **2001**, *36*, 373–380. [CrossRef]
20. Kreis, T. *Handbook of Holographic Interferometry: Optical and Digital Methods*; John Wiley & Sons: Hoboken, NJ, USA, 2006.
21. Hossain, M.M.; Mehta, D.S.; Shakher, C. Refractive index determination: An application of lensless Fourier digital holography. *Opt. Eng.* **2006**, *45*, 106203. [CrossRef]
22. Khodadad, D. Multiplexed Digital Holography Incorporating Speckle Correlation. Ph.D. Thesis, Luleå Tekniska Universitet, Luleå, Sweden, 2016.
23. Sharma, S.; Sheoran, G.; Shakher, C. Digital holographic interferometry for measurement of temperature in axisymmetric flames. *Appl. Opt.* **2012**, *51*, 3228–3235. [CrossRef]
24. Yuan, X.; Xue, Y.; Min, J.; Yu, X.; Li, M.; Li, R.; Yao, B. High-precision gaseous flame temperature field measurement based on quadriwave-lateral shearing interferometry. *Opt. Lasers Eng.* **2023**, *162*, 107430. [CrossRef]
25. Baffou, G. Wavefront microscopy using quadriwave lateral shearing interferometry: From bioimaging to nanophotonics. *ACS Photonics* **2023**, *10*, 322–339. [CrossRef]
26. Serrano-García, D.I.; Martínez-García, A.; Toto-Arellano, N.-I.; Otani, Y. Dynamic temperature field measurements using a polarization phase-shifting technique. *Opt. Eng.* **2014**, *53*, 112202. [CrossRef]

27. Wang, D.; Zhuang, T. The measurement of 3-D asymmetric temperature field by using real time laser interferometric tomography. *Opt. Lasers Eng.* **2001**, *36*, 289–297. [CrossRef]
28. Jabeen, N.; Nirala, A. Digital holographic interferometry for temperature measurement of oil lamp flames with different wick thicknesses. *Sustain. Energy Technol. Assess.* **2022**, *52*, 101964. [CrossRef]
29. Jabeen, N.; Nirala, A. Digital Holographic Interferometry for Temperature Measurement of Flame without Phase Unwrapping. *IETE J. Res.* **2021**, 1–10. [CrossRef]
30. Shoji, E.; Komiya, A.; Okajima, J.; Kawamura, H.; Maruyama, S. High-speed phase-shifting interferometry using triangular prism for time-resolved temperature measurement. *Appl. Opt.* **2015**, *54*, 6297–6304. [CrossRef]
31. Oprins, A.J.; Heynderickx, G.J.; Marin, G.B. Three-dimensional asymmetric flow and temperature fields in cracking furnaces. *Ind. Eng. Chem. Res.* **2001**, *40*, 5087–5094. [CrossRef]
32. Bååk, T. Thermal coefficient of refractive index of optical glasses. *JOSA* **1969**, *59*, 851–857. [CrossRef]
33. Doleček, R.; Psota, P.; Lédl, V.; Vít, T.; Václavík, J.; Kopecký, V. General temperature field measurement by digital holography. *Appl. Opt.* **2013**, *52*, A319–A325. [CrossRef]
34. Doleček, R.; Psota, P.; Lédl, V.; Vít, T.; Kopecký, V. Comparison of holographic setups used in heat and mass transfer measurement. In Proceedings of EPJ Web of Conferences; EDP Sciences: Les Ulis, France, 2014; Volume 67, p. 02021.
35. Khodadad, D. Phase-derivative-based estimation of a digital reference wave from a single off-axis digital hologram. *Appl. Opt.* **2016**, *55*, 1663–1669. [CrossRef] [PubMed]
36. Goodman, J.W. *Introduction to Fourier Optics*; McGraw-Hill: New York, NY, USA, 1968.
37. Khodadad, D.; Bergström, P.; Hällstig, E.; Sjödahl, M. Single shot dual-wavelength digital holography: Calibration based on speckle displacements. *Int. J. Optomechatronics* **2014**, *8*, 326–339. [CrossRef]
38. Born, M.; Wolf, E. *Principles of Optics: Electromagnetic Theory of Propagation, Interference and Diffraction of Light*; Elsevier: Amsterdam, The Netherlands, 2013.
39. Bengt, E. The Refractive Index of Air. *Metrologia* **1966**, *2*, 71. [CrossRef]
40. Bach, H.; Neuroth, N. *The Properties of Optical Glass*; Springer Science & Business Media: Berlin/Heidelberg, Germany, 1998.
41. Ciddor, P.E. Refractive index of air: New equations for the visible and near infrared. *Appl. Opt.* **1996**, *35*, 1566–1573. [CrossRef] [PubMed]
42. Schott, A. TIE-19: Temperature Coefficient of the Refractive Index. Mainz. 2016. Available online: https://www.schott.com/shop/medias/schott-tie-19-temperature-coefficient-of-refractive-index-eng.pdf?context=bWFzdGVyfHJvb3R8NDEzOTYzfGFwcGxpY2F0aW9uL3BkZnxoZWIvaDBlLzg4MTc0MDkyNjE1OTgucGRmfGY4MjM4MTMxNTU3Y2ZkMWYyODVjODNlM2ZmNTNkYmVlYTQ4ZmMxMjRjNjVmNTU0ZDhjODZmMTE3ODk2NmIyZDA (accessed on 1 May 2023).
43. Khodadad, D.; Bergström, P.; Hällstig, E.; Sjödahl, M. Fast and robust automatic calibration for single-shot dual-wavelength digital holography based on speckle displacements. *Appl. Opt.* **2015**, *54*, 5003–5010. [CrossRef] [PubMed]
44. Bergström, P.; Khodadad, D.; Hällstig, E.; Sjödahl, M. Dual-wavelength digital holography: Single-shot shape evaluation using speckle displacements and regularization. *Appl. Opt.* **2014**, *53*, 123–131. [CrossRef]
45. Leclercq, M.; Picart, P. A Robust Method for Full Chromatic Error Compensation in Digital Color Holography. In *Fringe 2013: 7th International Workshop on Advanced Optical Imaging and Metrology*; Springer: Berlin/Heidelberg, Germany, 2014; pp. 263–266.
46. Thomsen, M.; Fuentes, A.; Demarco, R.; Volkwein, C.; Consalvi, J.-L.; Reszka, P. Soot measurements in candle flames. *Exp. Therm. Fluid Sci.* **2017**, *82*, 116–123. [CrossRef]
47. Shan, L.; Huang, H.; Hong, B.; Zhao, J.; Wang, D.; Kong, M. Temperature measurement method of flame image fusion with different exposures. *Energies* **2020**, *13*, 1487. [CrossRef]
48. Zheng, S.; Ni, L.; Liu, H.; Zhou, H. Measurement of the distribution of temperature and emissivity of a candle flame using hyperspectral imaging technique. *Optik* **2019**, *183*, 222–231. [CrossRef]